Simultaneous NICER and NuSTAR Observations of the Ultracompact X-Ray Binary 4U 1543–624

R. M. Ludlam[1,10] , A. D. Jaodand[1] , J. A. García[1,2] , N. Degenaar[3], J. A. Tomsick[4] , E. M. Cackett[5] , A. C. Fabian[6] ,
P. Gandhi[7], D. J. K. Buisson[7], A. W. Shaw[8], and D. Chakrabarty[9]

[1] Cahill Center for Astronomy and Astrophysics, California Institute of Technology, Pasadena, CA 91125, USA; rmludlam@caltech.edu
[2] Remeis Observatory & ECAP, Universität Erlangen-Nürnberg, Sternwartstr. 7, D-96049, Bamberg, Germany
[3] Anton Pannekoek Institute for Astronomy, University of Amsterdam, Pastbus 94249, 1090 GE Amsterdam, The Netherlands
[4] Space Sciences Laboratory, 7 Gauss Way, University of California, Berkeley, CA 94720-7450, USA
[5] Department of Physics & Astronomy, Wayne State University, 666 West Hancock Street, Detroit, MI 48201, USA
[6] Institute of Astronomy, Madingley Road, Cambridge CB3 0HA, UK
[7] Department of Physics and Astronomy, University of Southampton, Highfield, Southampton, SO17 1BJ, UK
[8] Department of Physics, University of Nevada, Reno, NV 89557, USA
[9] MIT Kavli Institute for Astrophysics and Space Research, Massachusetts Institute of Technology, Cambridge, MA 02139, USA
Received 2020 December 7; revised 2021 March 8; accepted 2021 March 9; published 2021 April 26

Abstract

We present the first joint NuSTAR and NICER observations of the ultracompact X-ray binary (UCXB) 4U 1543 −624 obtained in 2020 April. The source was at a luminosity of $L_{0.5-50\,\mathrm{keV}} = 4.9(D/7\,\mathrm{kpc})^2 \times 10^{36}$ erg s^{-1} and showed evidence of reflected emission in the form of an O VIII line, Fe K line, and Compton hump within the spectrum. We used a full reflection model, known as XILLVERCO, that is tailored for the atypical abundances found in UCXBs, to account for the reflected emission. We tested the emission radii of the O and Fe line components and conclude that they originate from a common disk radius in the innermost region of the accretion disk ($R_{\mathrm{in}} \leqslant 1.07\,R_{\mathrm{ISCO}}$). Assuming that the compact accretor is a neutron star (NS) and the position of the inner disk is the Alfvén radius, we placed an upper limit on the magnetic field strength to be $B \leqslant 0.7(D/7\,\mathrm{kpc}) \times 10^8$ G at the poles. Given the lack of pulsations detected and position of R_{in}, it was likely that a boundary layer region had formed between the NS surface and inner edge of the accretion disk with an extent of 1.2 km. This implies a maximum radius of the neutron star accretor of $R_{\mathrm{NS}} \leqslant 12.1$ km when assuming a canonical NS mass of $1.4\,M_\odot$.

Unified Astronomy Thesaurus concepts: Accretion (14); Low-mass x-ray binary stars (939)

1. Introduction

Ultracompact X-ray binaries (UCXBs) are a subclass of low-mass X-ray binaries (LMXBs) with short orbital periods of $\lesssim 90$ minutes. The tight orbit of these systems means the compact object, either a neutron star (NS) or black hole (BH), is accreting via Roche-lobe overflow from a degenerate stellar companion, such as a white dwarf or He star (Nelson et al. 1986; Savonije et al. 1986). UCXBs are strong, persistent gravitational wave sources for future missions, such as NASA/ESA's LISA, that are sensitive in the sub-mHz regime (Nelemans & Jonker 2010).

The accretion disks in these systems differ from those of typical LMXBs since they are almost devoid of hydrogen while overabundant in oxygen, carbon, and/or neon (Nelemans et al. 2003). When accretion disks are externally illuminated by hard X-rays originating from close to the compact object, the photons are reprocessed and re-emitted as a series of atomic features superimposed onto a "reflected" continuum. These features are then broadened due to Doppler, special, and general relativistic effects in this region (Fabian et al. 2000). The strength of these effects depends on the proximity to the compact object; therefore, these reflection features can be used to infer fundamental properties of the compact object, as well as the accretion disk itself (e.g., Miller 2007; Cackett et al. 2008, 2009, 2010; Di Salvo et al. 2009, 2015; Papitto et al. 2009; Miller et al. 2013; Ludlam et al. 2017a).

In a typical accretion disk composed of solar abundance material, the Fe K line at 6.4–6.97 keV is the most prominent feature. However, in an UCXB, O VIII (∼0.65 keV) becomes dominant over Fe K (Ballantyne et al. 2002). It was previously thought that Fe emission should not be present in these systems since most of the ionizing radiation within the disk would be absorbed by the lower-Z atomic elements (Koliopanos et al. 2013). However, this was revealed not to be the case via XMM-Newton and Chandra observations of the UCXBs 4U 1543−624 and 4U 0614+091 (Madej & Jonker 2011; Madej et al. 2014). Indeed other UCXBs observed with XMM-Newton have since shown evidence of Fe emission lines (e.g., 4U 1728−34, 4U 1820−30, 4U 1916−05: Koliopanos et al. 2021a), although some detections are marginal (e.g., MAXI J0911−655: Sanna et al. 2017). Additionally, NuSTAR has observed reflection features in 4U 0614+091 (Ludlam et al. 2019a) and the recently classified UCXB IGR J17062-6143 (Degenaar et al. 2017; Strohmayer et al. 2018; van den Eijnden et al. 2018). The predicted absence of Fe emission in these systems was based on models that assume a cold, neutral disk and, therefore, any ionizing photons have a higher probability of being absorbed by the overabundant O atoms rather than Fe (see Figure 1 in Koliopanos et al. 2013). Yet the observational evidence of the Fe K line in UCXBs implies that the disk is hot and being illuminated in a similar manner to other accreting LMXBs (Madej et al. 2014).

4U 1543−624 is a UCXB with an orbital period of 18.2 ± 0.1 minutes (Wang & Chakrabarty 2004; Wang et al. 2015) located at a distance between $D \sim 1.4$–11.5 kpc (Wang & Chakrabarty 2004; Bailer-Jones et al. 2018; Serino et al.

2018). The nature of the compact object in 4U 1543−624 is uncertain, but very likely an NS from a tentative association with a Type-1 X-ray burst seen by MAXI (Serino et al. 2018) and its radio–X-ray behavior (Ludlam et al. 2017b, 2019b; Tetarenko et al. 2018). The degenerate companion in this system is a C/O or O/Ne white dwarf due to the absence of hydrogen and helium lines coupled with emission from carbon and oxygen in the optical spectrum (Nelemans et al. 2003).

As mentioned previously, the X-ray spectrum of 4U 1543 −624 has shown a broad O VIII Lyα emission feature at ∼0.7 keV in conjunction with Fe K emission (Juett & Chakrabarty 2003; Madej & Jonker 2011). Madej et al. (2014) presented an X-ray spectral analysis of 4U 1543−624 and 4U 0614+091 using a preliminary version of a new reflection model, XILLVERCO, that was tailored to accommodate the atypical elemental abundances in UCXBs. This model mimics the negligible H and He abundances in the disk by setting the abundance of metals to 10 times solar abundance and allowing for variable abundance of C and O. Though this only had a limited number of grid points (i.e., large steps between parameter values), spectral modeling using this initial XILLVER grid on 4U 1543−624 indicated an inner disk radius $<7.4\,R_g$ (where $R_g = GM/c^2$) and an inclination of $i \sim 65°$ (Madej et al. 2014).

More recently, Ludlam et al. (2019b) reported on NICER monitoring of 4U 1543−624 over a ∼10 day period in 2017 August while the source underwent a period of enhanced accretion activity with supplemental observations by Swift, INTEGRAL, and ATCA. The monitoring of this event allowed for tracking of changes in the accretion disk in this system. There was an increase in the strength of the thermal component at the lowest energies as the accretion disk moved closer to the NS (from $R_{in} > 60\,R_g$ to $R_{in} < 8\,R_g$ at peak intensity: Ludlam et al. 2019b). There was also a clear change in the shape and strength of the emission lines as well; however, this analysis simply used DISKLINE to model the emission lines from Fe and O rather than a full reflection spectrum framework leading to uncertainties regarding a common emission radius for these two features.

We present simultaneous observations of 4U 1543−624 with NICER and NuSTAR from 2020 April. This is the first time that NuSTAR has observed the source. The goal of these observations is to analyze the reflection spectrum in this system with a full reflection model to determine if the O and Fe components originate from similar disk radii and ionization. The combined passband of NICER and NuSTAR are ideal for revealing the presence of reflected emission while pinning down the continuum (Ludlam et al. 2020; Wang et al. 2020). We present the observations and data reduction in Section 2, our analysis in Section 3, and discuss the results in Section 4.

2. Observations and Data Reduction

NICER (Gendreau et al. 2012) observed 4U 1543−624 twice during the span of the contemporaneous NuSTAR observation. The first observation, ObsID 3604010101, began at 07:09:05 UT on 2020 April 19 for an exposure of 9.1 ks. The second observation, ObsID 3604010102, began at 00:33:20 UT on 2020 April 20 for 863 s. The NICER observations were reduced using NICERDAS 2020-04-23_V007a. Data were recalibrated with the latest calibration files available in CALDB release 20200722 through implementation of the NICERL2 command. Good time intervals (GTIs) were generated using
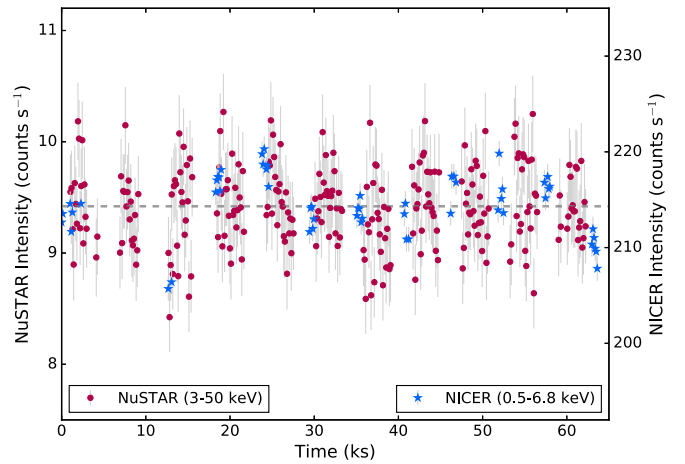

Figure 1. Light curve for the NuSTAR /FPMA (circles) and NICER (stars) observations of 4U 1543−624 binned to 128 s. The gray dashed line indicates the average count rate for both NuSTAR and NICER. The time elapsed is from the start of the NICER observation on 2020 April 19 at 07:12:55UT. The source exhibits ≲10% variability over the course of the observation. Only one FPM is shown for clarity.

NIMAKETIME to select events that occurred when the particle background was low (KP < 5 and COR_SAX > 4) and avoiding times of extreme optical light loading (SUN_ANGLE > 60 and FPM_UNDERONLY_COUNT < 200).[11] Using NIEXTRACT-EVENTS, the GTIs were applied to the data. The resulting event files were loaded into XSELECT to extract a combined spectrum and light curves in various energy bands. Background spectra were generated using the nibackgen3C50v6[12] tool (R. Remillard 2021, in preparation) for each cleaned and ufa (calibrated but unfiltered) event file pair based on instrument proxies to account for the observing conditions at the time. These were then combined into a single background spectrum that was weighted by the duration of each cleaned event file using MATHPHA. We use the standard public RMF and the on-axis average ARF in CALDB v.20200722 when modeling the NICER spectrum.

NuSTAR (Harrison et al. 2013) observed 4U 1543−624 on 2020 April 19 starting at 07:21:09 UT. ObsID 30601006002 contains ∼32.3 ks of data from Focal Plane Module (FPM) A and ∼32.1 ks from FPMB. The NuSTAR data were reduced using the standard data reduction process with NUSTARDAS v1.9.2 and CALDB 20191219. Spectra and light curves are extracted using a circular region with an 80″ radial centered on the source. Backgrounds were generated from an 80″ radial region on the same detector but away from the source.

There were no Type-I X-ray bursts present in either data set; therefore, no further filtering was needed. Systematic errors of 1% in the 2–10 keV band and 5% in the 0.3–2 keV band were added to the NICER spectrum (Alabarta et al. 2020). The NuSTAR spectra were binned by three PI channels using GRPPHA (Choudhury et al. 2017). Figure 1 shows the NuSTAR/FPMA (circles) and NICER (stars) light curves binned to 128 s starting from when NICER began observing 4U 1543−624. The source exhibits ≲10% variability over the ∼65 ks of elapsed time since the start of the observations. Using the definitions from Bult et al. (2018), we compare the

---

[11] See Bogdanov et al. (2019) regarding information on the NICER screening flags.
[12] https://heasarc.gsfc.nasa.gov/docs/nicer/tools/nicer_bkg_est_tools.html
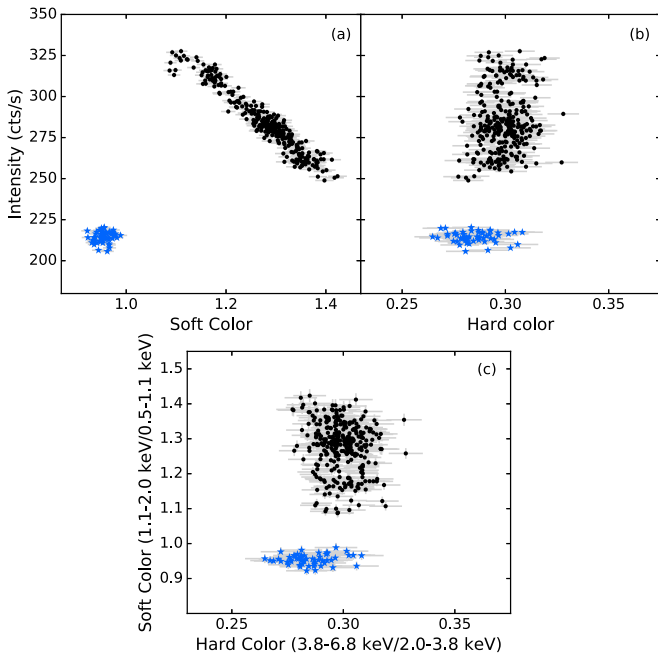
Figure 2. A comparison of the NICER observations of 4U 1543−624 during the 2017 outburst (black circles) reported in Ludlam et al. (2019b) to the observations obtained in 2020 (blue stars) for (a) the soft color vs. the source intensity in the 0.5–6.8 keV band, (b) the hard color vs. intensity, and (c) the soft color vs. the hard color. The new observations probe different regions on these planes.
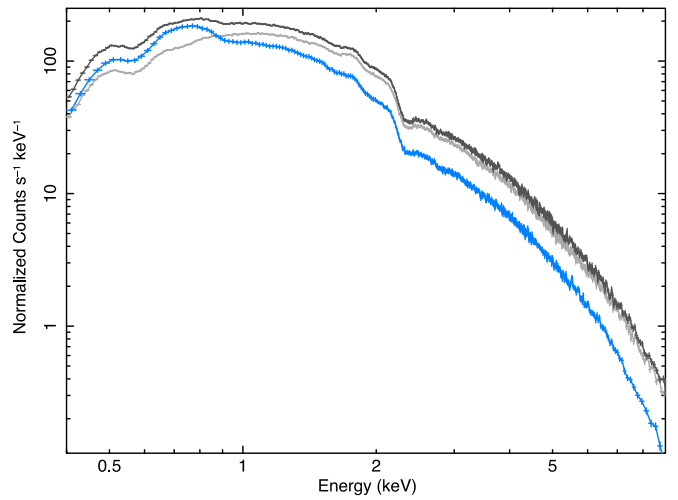

Figure 3. Comparison of the 0.4–9 keV counts spectra for the NICER observations reported here (blue) and the observations from 2017 intervals A (light gray) and E (dark gray) from Ludlam et al. (2019b). The source is at a lower flux in 2020 in comparison to the previous NICER observations.

NICER hard color (3.8–6.8 keV/2.0–3.8 keV) and soft color (1.1–2.0 keV/0.5–1.1 keV) of 4U 1543−624 to the previous observations that occurred in 2017 August during an enhanced accretion period in Figure 2. The 2020 observations presented here captured the source at a lower intensity. For comparison, we also show the counts spectrum in Figure 3 for the 2020 NICER observations to intervals A and E from Ludlam et al. (2019b).

Furthermore, we search the data for pulsations in Section 3.2. The data obtained for both NICER and NuSTAR were barycentered to the solar system barycenter using the source position prior to the search. We used the same source regions as previously mentioned to extract source photons in the 3–78 keV energy band from the NuSTAR observations. NICER photons were extracted from the 0.3–10 keV energy band. Note that NICER is not an X-ray imaging mission, therefore there is no need for an extraction region. Events were extracted using the same GTIs as were used for extracting spectra. However, the NuSTAR FPMA and FPMB can have GTI mismatches (Bachetti et al. 2015), hence we trimmed each GTI interval to be within a safe range of 100–300 s. We applied clockfile V.108, generated by using NUSTAR-CLOCK-UTILS,[13] to the NuSTAR event files using the FTOOL BARYCORR. The clockfile v.108 corrects for both the NuSTAR clock variations and absolute timing uncertainty of 5 μs between NuSTAR and NICER.

3. Analysis and Results

3.1. Spectral

The spectral analysis was conducted using XSPEC v.12.11.0 (Arnaud 1996). The NICER data were modeled in the

0.4–9 keV band, whereas the NuSTAR data were considered in the 3–40 keV energy range. Data above these energy ranges are dominated by the X-ray background. A constant was allowed to vary for the NuSTAR /FPMB and NICER spectra, while the NuSTAR /FPMA is fixed at 1.0, to allow for cross-calibration differences. The absorption along the line of sight was accounted for with the TBABS model (Wilms et al. 2000). There were two narrow features in the low-energy portion of the NICER spectrum that were also seen in Ludlam et al. (2020) for a different source, 4U 1735 − 44. These are likely astrophysical in origin, i.e., due to the neutral interstellar medium (ISM) along the line of sight (Pinto et al. 2013), although instrumental uncertainties are also a plausible explanation. We added two EDGE components with energies bound between 0.5–0.6 keV and 0.8–0.9 keV to account for the features.

The continuum was modeled according to the framework of Lin et al. (2007) in order to provide a direct comparison to the results in the previous analysis on 4U 1543−624 using NICER observations (Ludlam et al. 2019b; Koliopanos et al. 2021b). A simple absorbed cutoff power law to account for weak Comptonizaton from the corona and single-temperature thermal component originating from a boundary layer or NS surface were sufficient to describe the continuum spectra. The model parameters and values are reported in Table 1, and Figure 4 shows the ratio of the data to the continuum model. The photon index, Γ, is softer and the single-temperature blackbody is hotter in comparison to the 2017 observations reported in Ludlam et al. (2019b) ($\Gamma \leqslant 1.86$, $kT_{bb} < 0.83$ keV). However, the thermal component is cooler than the value reported in Koliopanos et al. (2021b) ($kT_{bb} \sim 1.8$ keV). The data do not require a disk component suggesting that the thermal emission from the disk is cooler than when the source was observed in 2017 during an enhanced accretion episode.

We switch the empirical continuum model for a more physically motivated model. When using NTHCOMP to account for Comptonized accretion instead of the cutoff power law that would arise from the corona, we find $\Gamma = 2.4 \pm 0.1$, seed photon temperature $kT_{bb} = 1.04^{+0.02}_{-0.03} \times 10^{-1}$ keV, a high-energy rollover that tends to the upper limit to 1000 keV, and

---

[13] https://github.com/nustar/nustar-clock-utils

Table 1
Joint NICER and NuSTAR Spectral Modeling

Model	Parameter	Continuum	DISKLINE		XILLVERCO		
			D1	D2	X1	X2	X3
CONSTANT	C_{FPMB}	1.02 ± 0.01	1.01 ± 0.01	1.01 ± 0.01	1.01 ± 0.01	1.01 ± 0.01	1.01 ± 0.01
	C_{NICER}	1.02 ± 0.01	1.03 ± 0.01	1.01 ± 0.01	1.03 ± 0.01	1.03 ± 0.01	1.03 ± 0.01
TBABS	N_H (10^{21} cm^{-2})	$3.35^{+0.02}_{-0.01}$	3.22 ± 0.01	$3.20^{+0.01}_{-0.02}$	3.45 ± 0.02	3.45^*	$3.36^{+0.03}_{-0.02}$
EDGE	E (keV) (10^{-1})	5.2^*	$5.10^{+0.08}_{-0.02}$	5.20 ± 0.01	5.20 ± 0.01	$\cdots$	$5.13^{+0.04}_{-0.05}$
	τ_{max} (10^{-1})	$3.2 \pm 0.8 \times 10^{-7}$	0.657 ± 0.01	$0.57^{+0.01}_{-0.02}$	$1.15^{+0.03}_{-0.02}$	$\cdots$	1.09 ± 0.04
EDGE	E (keV) (10^{-1})	8.78 ± 0.02	$8.88^{+0.06}_{-0.03}$	$8.89^{+0.06}_{-0.04}$	$8.53^{+0.03}_{-0.04}$	$\cdots$	$8.54^{+0.03}_{-0.04}$
	τ_{max} (10^{-1})	3.39 ± 0.07	$1.87^{+0.01}_{-0.02}$	$1.88^{+0.02}_{-0.08}$	2.61 ± 0.03	$\cdots$	$2.37^{+0.03}_{-0.02}$
BBODY	kT (keV)	1.44 ± 0.01	1.31 ± 0.01	1.27 ± 0.01	1.29 ± 0.01	$1.30^{+0.02}_{-0.01}$	$1.29^{+0.03}_{-0.01}$
	norm$_{bb}$ (10^{-3})	1.05 ± 0.02	1.01 ± 0.01	$0.98^{+0.03}_{-0.02}$	1.02 ± 0.02	$1.08^{+0.01}_{-0.04}$	$0.97^{+0.02}_{-0.01}$
	$R_{bb,\ sph}$ (km)	2.78 ± 0.06	3.30 ± 0.04	$3.45^{+0.11}_{-0.07}$	3.42 ± 0.07	$3.46^{+0.06}_{-0.13}$	$3.33^{+0.10}_{-0.04}$
CUTOFFPL	Γ	2.41 ± 0.01	2.34 ± 0.01	2.33 ± 0.01	2.31 ± 0.01	2.34 ± 0.01	2.26 ± 0.01
	E_{cutoff} (keV)	176 ± 8	152 ± 2	148 ± 3	99^{+7}_{-5}	137 ± 7	74 ± 1
	norm$_{pl}$ (10^{-1})	1.82 ± 0.01	1.64 ± 0.01	$1.62^{+0.01}_{-0.02}$	1.30 ± 0.03	$1.43^{+0.03}_{-0.07}$	$1.09^{+0.02}_{-0.04}$
DISKLINE$_1$	E_O (10^{-1} keV)	$\cdots$	$6.88^{+0.02}_{-0.06}$	$6.87^{+0.03}_{-0.02}$	$\cdots$	$\cdots$	$\cdots$
	$|q|$	$\cdots$	$2.38^{+0.07}_{-0.01}$	2.41 ± 0.02	$\cdots$	$\cdots$	$\cdots$
	i (°)	$\cdots$	$52.3^{+1.2}_{-0.3}$	53 ± 1	$\cdots$	$\cdots$	$\cdots$
	R_{in} (R_g)	$\cdots$	$6.02^{+0.20}_{-0.02}$	$\dagger 6.01^{+0.20}_{-0.01}$	$\cdots$	$\cdots$	$\cdots$
	R_{in} (km)	$\cdots$	$12.44^{+0.40}_{-0.04}$	$\dagger 12.42^{+0.41}_{-0.02}$	$\cdots$	$\cdots$	$\cdots$
	norm$_{line1}$ (10^{-2})	$\cdots$	$1.61^{+0.05}_{-0.01}$	1.58 ± 0.01	$\cdots$	$\cdots$	$\cdots$
DISKLINE$_2$	E_{Fe} (keV)	$\cdots$	$6.40^{+0.03}_*$	$6.41^{+0.04}_{-0.01}$	$\cdots$	$\cdots$	$\cdots$
	R_{in} (R_g)	$\cdots$	$12.32^{+0.02}_{-0.05}$	$\dagger 6.01^{+0.20}_{-0.01}$	$\cdots$	$\cdots$	$\cdots$
	R_{in} (km)	$\cdots$	$25.46^{+0.04}_{-0.10}$	$\dagger 12.42^{+0.41}_{-0.02}$	$\cdots$	$\cdots$	$\cdots$
	norm$_{line2}$ (10^{-4})	$\cdots$	$3.40^{+0.18}_{-0.03}$	$3.9^{+0.2}_{-0.1}$	$\cdots$	$\cdots$	$\cdots$
RELCONV	q	$\cdots$	$\cdots$	$\cdots$	2.4 ± 0.1	2.0 ± 0.2	$2.55^{+0.02}_{-0.03}$
	i (°)	$\cdots$	$\cdots$	$\cdots$	53^{+2}_{-1}	53^{+1}_{-2}	53 ± 1
	R_{in} (R_{ISCO})	$\cdots$	$\cdots$	$\cdots$	1.02 ± 0.01	$1.03^{+0.04}_{-0.03}$	$1.02^{+0.03}_{-0.01}$
	R_{in} (R_g)	$\cdots$	$\cdots$	$\cdots$	6.12 ± 0.06	$6.18^{+0.24}_{-0.18}$	$6.12^{+0.18}_{-0.06}$
	R_{in} (km)	$\cdots$	$\cdots$	$\cdots$	12.7 ± 0.1	$12.8^{+0.5}_{-0.4}$	$12.7^{+0.4}_{-0.1}$
XILLVERCO	A_{CO}	$\cdots$	$\cdots$	$\cdots$	4.3 ± 0.1	$4.3^{+0.2}_{-0.1}$	4.0 ± 0.1
	kT_{disk} (10^{-2} keV)	$\cdots$	$\cdots$	$\cdots$	$5.02^{+0.02}_{-0.01}$	$5.01^{+0.03}_{-0.01}$	5.01 ± 0.01
	Frac$_{PL/BB}$ (10^{-1})	$\cdots$	$\cdots$	$\cdots$	1.18 ± 0.02	$1.15^{+0.09}_{-0.07}$	$1.51^{+0.02}_{-0.03}$
	norm$_{xillver}$ (10^{-8})	$\cdots$	$\cdots$	$\cdots$	2.49 ± 0.05	2.0 ± 0.1	$2.31^{+0.06}_{-0.03}$
	χ^2 (dof)	4935 (1462)	1732 (1453)	1748 (1454)	1814 (1454)	1613 (1408)	1355 (1101)

Note. Errors are reported at the 90% confidence level and calculated from Markov Chain Monte Carlo (MCMC) of chain length 10^6. NICER is fit in the 0.4–9 keV energy band while NuSTAR is fit in the 3–40 keV band. A multiplicative constant is used on the NICER and FPMB data, while FPMA is fixed to unity. The spherical blackbody radius is calculated assuming a distance of 7 kpc and color-correction factor of 1.7 (Shimura & Takahara 1995). The emissivity index and inclination are tied between the two DISKLINE components. D1 allows the inner disk radii to differ between the two DISKLINE components, whereas D2 assumes a common emission radius for both lines. The outer disk radius is fixed at 990 R_g and the dimensionless spin parameter is set to $a_* = 0$ (hence, 1 $R_{ISCO} = 6\ R_g = 12.4$ km). The photon index and high-energy cutoff in the XILLVERCO model are tied to the values of the continuum power-law component. X1 is the full passband from 0.4 to 40 keV, X2 is ignoring the O VIII line by ignoring below 0.9 keV and fixing the column density and low-E edges, and X3 uses the 0.4–40 keV band but ignores the Fe line region from 5 to 8 keV. * = fixed, $\dagger$ = tied.

normalization of norm $= 1.74^{+0.02}_{-0.01} \times 10^{-1}$. This is similar in shape to the cutoff power-law component in the previous continuum model description, but predicts photons out to higher energy that we are not sensitive to with the current data. We note that the high-energy rollover also tended to 1000 keV when NTHCOMP was applied to the NICER and INTEGRAL observations of 4U 1543−624 (Ludlam et al. 2019b). The fit still requires a single-temperature blackbody component of $kT = 1.43 \pm 0.01$ keV and norm $= 1.01^{+0.01}_{-0.02} \times 10^{-3}$. The edges and multiplicative constants are similar to the continuum values reported in Table 1 with a slightly lower value for N_H ($3.20 \pm 0.02 \times 10^{21}$ cm^{-2}), but this is likely a more reliable measure of the column density given that the NTHCOMP has a low-energy turnover that the power-law component lacks (which can lead to a higher inferred N_H value in the latter case).

However, the N_H values between the two continuum models are not largely discrepant. The reduced χ^2 is upwards of 2.8 (χ^2/dof $= 4236/1464$), but statistically better than the simple continuum model description. However, there currently do not exist reflection models that are tailored to the atypical abundances observed in the accretion disks of UCXBs using a Comptonized or blackbody illuminating continuum. Therefore, while we report the model parameter values using NTHCOMP for completeness, we do not pursue this further when modeling the reflected emission.

Fitting the emission lines with simple Gaussian components provides an equivalent width of ∼39 eV for the O VIII near 0.7 keV and ∼143 eV for the Fe K emission at 6.4 keV. These are consistent with the values reported in Ludlam et al. (2019b). For direct comparison to Ludlam et al. (2019b), we add two
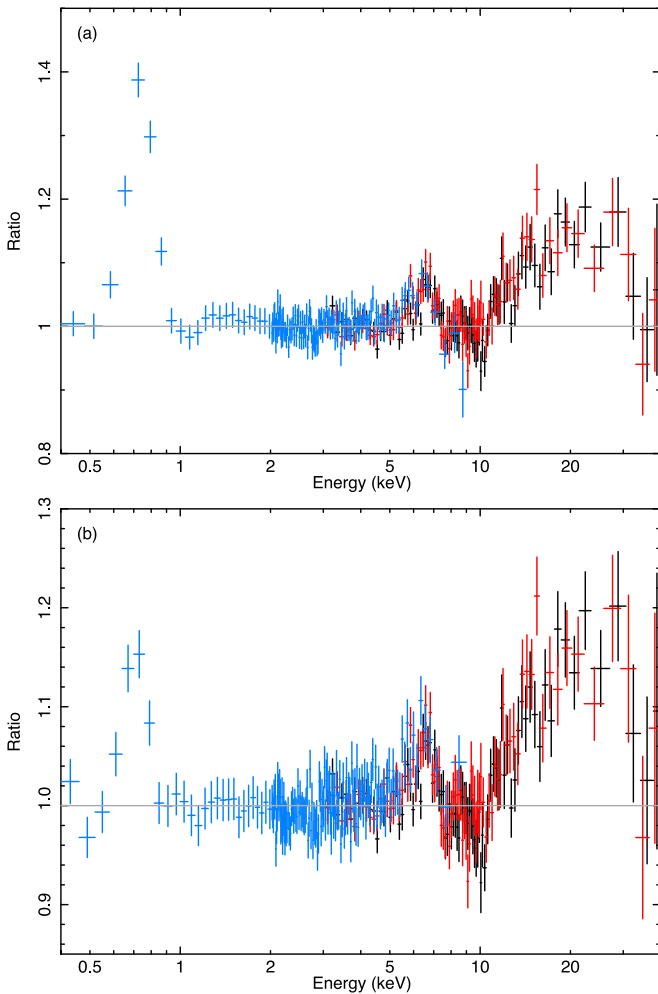
Figure 4. Ratio of the NICER (blue) and NuSTAR (FPMA: black, FPMB: red) data to the simple continuum model of an absorbed blackbody and power law (a) without the two edge components and (b) with the edges added. A prominent O emission line is present ~0.7 keV, as well as a Fe K line ~6.4 keV and a Compton hump at the highest energies. These regions were ignored when fitting the continuum to prevent these features from skewing the fit. Data were rebinned for plotting purposes.

DISKLINE (Fabian et al. 1989) components to account for the O VIII and Fe K lines with energies between 0.6–0.7 keV and 6.4–6.97 keV, respectively. The inclination (i) and emissivity index ($|q|$) parameters are tied between the line components. In the first instance, we allow the inner disk radius to differ between components. This is reported in Table 1 under D1. The emitting radius of the Fe line is further out in the disk than the O VIII line, which is consistent with the results reported in Ludlam et al. (2019b) when R_{in} is allowed to differ. In the second case, we tie the inner disk radius between the two lines, which is reported under D2 in Table 1. In this case, the emission region of both lines is from the innermost accretion disk within $\leqslant 6.21\,R_g$, which agrees with the inferred inner disk radius from interval E ($<8.7\,R_g$, Ludlam et al. 2019b) and suggests that the disk has not receded after the peak flux observed in 2017. For both spectral fits, the emissivity index is consistent with values reported in Madej et al. (2014) and observed in other NS LMXBs such as 4U 1705−44, 4U 1636 −53, 4U 1702−429, Serpens X-1, as well as the UCXB 4U 0614+091 (Egron et al. 2013; Ludlam et al. 2017a, 2018, 2019a). Additionally, the inclination is lower

($i \sim 53°$) than has been reported previously for this source, but in agreement with the inclination inferred from the optical observation (Wang & Chakrabarty 2004).

It is important to note that while using DISKLINE is acceptable as a preliminary diagnostic for line emission, the profile assumes a single emission line is being broadened by Doppler and relativistic effects. This does not account for the blending of emission from other atomic species or energy levels within the energy region of interest for the emission lines (e.g., the blending of Fe XXV and Fe XXVI K$_\alpha$, O VIII Lyα, and β, or even emission of Mg blended with Fe L as shown in Ludlam et al. 2018). The full reflection spectrum is a series of atomic features that are superimposed onto a reprocessed continuum that is then broadened. Hence, a complete reflection model should be utilized when performing spectral modeling of reflection.

We opt for a more consistent approach to describe the reflection spectrum present within the system by using a modified version of XILLVER (García et al. 2013) that accounts for the unusual elemental abundances in the accretion disk, known as XILLVERCO. This assumes that coronal emission is illuminating the accretion disk as a power law, Γ, with a high-energy cutoff, E_{cutoff}. The reflection model also contains emergent thermal emission from the accretion disk itself, kT_{disk}, at the location where the emission features arise. The Frac parameter adjusts the strength of the power law illuminating the disk relative to blackbody arising from the disk (σT^4), Frac = Flux$_{PL}$(10^2–10^6 eV)/Flux$_{BB}$(0.1–10^6 eV). This is an updated version of the model used in Madej et al. (2014). The earlier grid calculations had set the abundances of all elements to be 10 times those from Lodders (2003), except for H and He (which were left at solar abundance), and in the case of C and O to 100 times the abundance from Lodders (2003). Here, the updated table of the XILLVERCO model has the abundances set as follows: H and He to 0.1 times solar abundance from Lodders (2003), C and O are allowed to vary using the A_{CO} parameter, and all other elements are set to solar abundance. This model also has over 10^5 more spectral grid points than the initial model used in Madej et al. (2014).

When using XILLVERCO, we tie the photon index and high-energy cutoff to those in the continuum power-law component for consistency. The reflection component is convolved with RELCONV (Dauser et al. 2010) to account for broadening due to different effects within the innermost region of the accretion and proximity to the NS. We tie the inner and outer emissivity index in order to create a single illumination profile, q. The outer disk radius is set to $990\,R_g$ and the dimensionless spin parameter is fixed at $a_* = 0$.

Applying this model to the full 0.4–40 keV, we achieve an improved fit of $\Delta\chi^2 = 3121$ for 8 degrees of freedom (dof) in comparison to the continuum fit. The values for each parameter are shown in Table 1 under X1. While the statistical fit may be worse than the overall model using DISKLINE components, using XILLVERCO provides more information regarding the emitting material (e.g., abundance of C/O) and correctly accounts for the reprocessed continuum emission. The unfolded model and residuals divided by the error are shown in Figure 5. Note that the discrepancy above 6 keV between NICER and NuSTAR data was also reported in Ludlam et al. (2020) when fitting simultaneous data from both missions. This has to do with the difference in calibration between missions (see Ludlam et al. 2020 for a more detailed discussion).
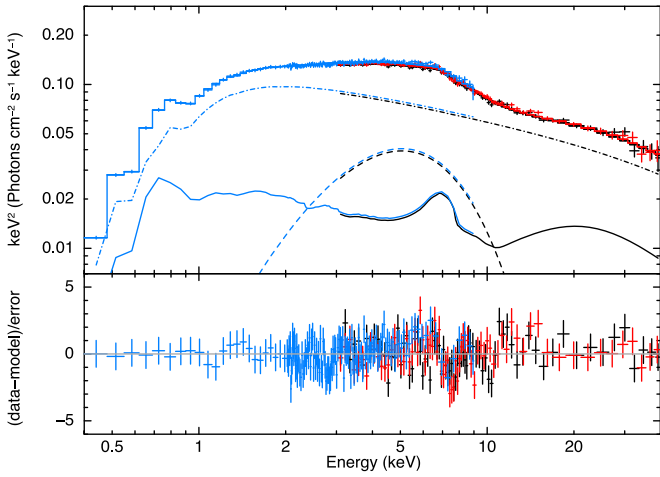
Figure 5. The unfolded spectrum with model components for the NICER (blue) and NuSTAR (FPMA: black, FPMB: red) data for the reflection modeling reported in Table 1. The dashed line indicates the single-temperature blackbody, the dotted–dashed line is the power-law component, the solid line is the reflection component from XILLVERCO.

Figure 6. Best-fit reflection model reported in Table 1 at 1.02 $R_{\rm ISCO}$ (solid line) and contrasting 100 $R_{\rm ISCO}$ (dashed line) overlaid on the NICER data to highlight the broad O line component. The larger inner disk radius relaxes the relativistic effects to show the local rest-frame emission. The O VIII Lyα and β components can be seen when relativistic effects are removed. For clarity, the data were rebinned.

The disk is close to the innermost stable circular orbit ($R_{\rm in} = 1.02 \pm 0.01\, R_{\rm ISCO}$) and the inclination is consistent with the values inferred from the DISKLINE modeling ($i \sim 53°$). Figure 6 shows the O VIII line with the blurred reflection model at the best-fit inner disk radius overlaid. For reference, we have also plotted the reflection model at a large radius to remove the relativistic effects. The O VIII Lyα and β components become evident when relativistic effects are relaxed. The abundance of C/O is about 10 times less than the values reported by Madej et al. (2014) when using the previous version of XILLVERCO, but it is important to note that the abundances in that model were set up 10 times larger. Therefore the values obtained for the C/O abundance are consistent. The Frac parameter is in agreement with the value reported in Madej et al. (2014). The thermal emission from the accretion disk is indeed cooler (~ 0.05 keV) than during the 2017 NICER observations at peak intensity (~ 0.1 keV: Ludlam et al. 2019b).

To check if this lower disk temperature is consistent with not being able to detect the accretion disk component in the continuum modeling, we add a DISKBB component to the continuum description with $kT = 0.05$ keV and the normalization value equivalent to the inner edge of the accretion disk inferred from reflection modeling (norm$_{\rm disk} = 26$ for $i = 53°$, $D = 7$ kpc, and a color-correction factor of 1.7). The DISKBB component accounts for less than 0.00001% of the photons at 0.5 keV, which is consistent with not being statistically needed during the simple continuum modeling. We can also calculate the expected thermal flux from the XILLVERCO model itself that would be expected for a distant observer. The expected unabsorbed thermal flux at 7 kpc in the 0.1–10^6 eV band would be $F_{\rm xillverCO,BB,7\,kpc} = 2.11 \times 10^{-14}$ erg cm^{-2} s^{-1}. For comparison, the unabsorbed continuum flux from the source in the same energy band using "energies extend" command in XSPEC is $F_{\rm continuum,0.1-10^6\,eV} \simeq 3.53 \times 10^{-8}$ erg cm^{-2} s^{-1}. This is the same order of magnitude contribution as the check using DISKBB and consistent with the disk component not being detected in the overall continuum model.

To check if these line components originate from a concurrent radius in the accretion disk or different radii, we model the spectra by fixing the absorption column and removing the O VIII line by ignoring below 0.9 keV so that
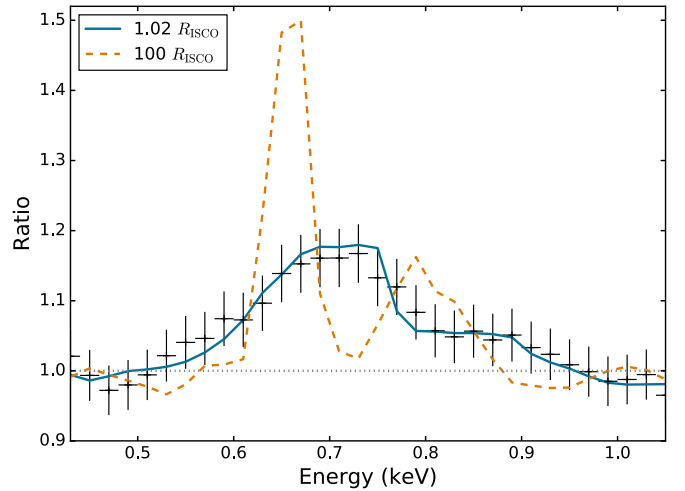
the fit will be driven by the Fe line (X2 in Table 1). This provides a position on the inner disk radius of $R_{\rm in} = 1.03^{+0.04}_{-0.03}\, R_{\rm ISCO}$ from fitting the reflection emission without the O line. Conversely, we also fit the spectrum from 0.4 to 40 keV but ignore the Fe band from 5 to 8 keV to see what constraints are returned from the O line (X3 in Table 1). This gives an inner disk of $R_{\rm in} = 1.02^{+0.03}_{-0.01}\, R_{\rm ISCO}$. The emission radii inferred from each line are consistent within the 90% confidence level, supporting a common emission radius in this system as was suggested from the line profiles plotted in velocity space (see Figure 5 of Ludlam et al. 2019b).

3.2. Timing

We searched the NICER and NuSTAR data for coherent pulsations that would provide further support for an NS accretor in this system. We utilized the HENDRICS package within the powerful Python X-ray timing software STINGRAY (Huppenkothen et al. 2019) to search for pulsations. Light curves binned with 0.001 s, 1 s, and 10 s were generated via HENCALIBRATE and HENLCURVE to check for any variations or nonstationary processes within the light curve, but none were found. We proceeded to split the (unbinned) time-series events into chunks of one-tenth the orbital period in order to conduct a search for pulsations. In the case of highly compact binaries, Doppler effects due to orbital motion varies the pulse frequency and spreads power over multiple frequency bins. To mitigate this, a constant acceleration model was used to account for the orbital motion (as outlined in Ransom 2001; Ransom et al. 2002) and searches were conducted over various possible acceleration values. The maximum acceleration value for these searches is given by Acc $= \frac{z\,c}{f\,T^2}$, where z is the acceleration search depth ($z = \dot{f} \times T^2$), c is the speed of light, f is the pulse frequency, and T is the observation duration. We therefore split the time series into 150 s chunks and then, assuming a bin depth of $z = 10$ and maximal pulse frequency of 800 Hz (which would be more rapid than the fastest known millisecond pulsar, PSR J1748−2446ad: Hessels et al. 2006), we conducted the constant acceleration search. The

acceleration searches do not yield any significant candidate for coherent pulsations.

4. Discussion

We present the first NuSTAR observation of the ultracompact X-ray binary 4U 1543−624 that was coordinated with NICER. The source was in a lower flux state than previously observed by NICER during the 2017 enhanced accretion phase. The 0.5–50 keV luminosity was $L_{0.5-50\,\mathrm{keV}} = 4.9(D/7\,\mathrm{kpc})^2 \times 10^{36}$ erg s^{-1}, which is 42% of the peak luminosity during the 2017 brightening. At this luminosity, the source has a mass accretion rate of $\dot{m} = 4.3 \times 10^{-10}\ M_\odot$ yr^{-1}. The source exhibited strong emission features due to the reprocessing of direct continuum emission by the accretion disk. Fitting the reflection spectrum with a model tailored to the atypical abundances found in these systems, XILLVERCO, we test the emission radii of the O VIII and Fe line components. We find a common emission radius for both line features of $R_{\rm in} < 1.07\,R_{\rm ISCO}$, indicating that the disk remains close to the compact object. There are other systems where the accretion disk is consistent with the innermost stable circular orbit at different flux levels and spectral states (e.g., 1RXS J180408.9−34205: Degenaar et al. 2016; Ludlam et al. 2016), so while 4U 1543−624 is not unique in this regard, it is interesting that the disk has not receded after the peak intensity observed in 2017.

Given the amount of evidence supporting an NS accretor in this system (e.g., tentative association with a Type-I X-ray burst: Serino et al. 2018; X-ray–Radio luminosity: Ludlam et al. 2019b), we discuss the results of the spectral modeling in the context of the source being an NS. The measured position of the inner disk radius from XILLVERCO corresponds to 12.4–13.3 km when assuming a canonical NS mass of 1.4 $M_\odot$. The upper limit on the inner disk position ($R_{\rm in} = 6.42\,R_g$) and 0.5–50 keV unabsorbed flux of $F_{\rm unabs} = 8.4 \times 10^{-10}$ erg cm^{-2} s^{-1} places an upper limit on the dipolar magnetic field of $B \leqslant 0.7(D/7\,\mathrm{kpc}) \times 10^8$ G at the poles, using Equation (1) in Ludlam et al. (2020). This is within the range estimated from the 2017 enhanced accretion event and further supports a weak B-field in this system. Additionally, this is consistent with the range of magnetic field strengths estimated in Mukherjee et al. (2015) for accreting millisecond X-ray pulsars (AMXPs), though no pulsations have been detected for this system.

Given the lack of pulsations detected and the small inner disk radius inferred from the reflection features, it does not appear that material is being channeled along magnetic field lines onto the surface of the NS, but rather that the accreting material forms a boundary layer region between the disk and NS surface. This would correspond to the single-temperature thermal component in the spectral modeling. The normalization of the blackbody component suggests a compact emission region of 3.4 km at 7 kpc and using a color-correction factor of 1.7 (Shimura & Takahara 1995). However, this conversion assumes spherical emission rather than banded emission from the NS surface. Accounting for a narrow equatorial banded region with a vertical height that is 5%–10% of the radius (Popham & Sunyaev 2001) can easily increase this blackbody emission radius to $R_{\rm BB} \sim 11$–15 km. Equation (25) from Popham & Sunyaev (2001) allows us to estimate the size of the boundary layer region normal to the NS surface given the mass accretion rate of $\dot{m} = 4.3 \times 10^{-10} M_\odot$ yr^{-1} at the time of

the observation. This corresponds to a boundary layer with a radial extent of $R_{\rm BL} = 1.2$ km from the NS surface. This estimate combined with the position of the inner edge of the accretion disk places an upper limit on the radial extent of the NS of $R_{\rm NS} \leqslant 12.1$ km for $M_{\rm NS} = 1.4\,M_\odot$, if indeed the compact object is an NS in this system.

Koliopanos et al. (2021b) recently looked at the presence of the Fe line feature in 4U 1543−624 over a 20 year period from RXTE (1997), Chandra (2000), XMM-Newton (2001), and NICER (2017). The source was in a soft state for all the observations that were analyzed with a 0.5–30 keV luminosity (at 7 kpc) ranging from 5.1×10^{36} erg s^{-1} to 6.7×10^{36} erg s^{-1}. The Fe line was clearly present in the RXTE and NICER data, but not detected in the XMM-Newton or Chandra observations. Given the small range in luminosity and the consistency of spectral parameter values obtained across missions, the disappearance of the Fe line component is attributed to microscopic processes in the disk rather than macroscopic changes (Koliopanos et al. 2021b). Though the observations presented here occurred at a lower 0.5–30 keV luminosity of ~4.76 $(D/7\,\mathrm{kpc})^2 \times 10^{36}$ erg s^{-1}, we see a strong Fe line component. The concurrent strong O line indicates that the oxygen in the disk is not fully ionized but rather only partially ionized, yet we do not see screening effects that are predicted to quench the Fe line as per Koliopanos et al. (2013).

Though the ionization is not explicitly returned as a parameter by the XILLVERCO model, we can estimate the ionization state of the emitting material via $\xi = 4\pi F_x/n$ (as is defined for all XILLVER models; García et al. 2013), where F_x is the ionizing flux from 0.1 to 1000 keV and n is the number density of the material in the disk. The XILLVERCO model has a hard-coded disk number density of $n = 10^{17}$ cm^{-3} (Madej et al. 2014). Using this hard-coded disk number density and that $F_x = {\rm Flux}_{\rm PL} = {\rm Frac}(\sigma T^4)$ by model definition, then $\log(\xi/[\mathrm{erg\ cm\ s}^{-1}]) \simeq 1.9$–2.1. This is in line with the emitting material being partially ionized rather than fully ionized, but should be considered a lower limit on the ionization state of the material given that illuminating blackbody X-rays from the boundary layer are not included in the model definition of ξ.

Ideally, when modeling the reflection emission in these systems, we would like to be able to account for illumination from the boundary layer or NS surface in addition to the coronal emission. We are currently working to expand the XILLVERCO model to account for irradiation of the accretion disk by both components, tracking the ionization, and higher disk density. However, these initial results with the current XILLVERCO model with additional grid points and a more realistic handling of the atypical abundance in these systems than the preliminary grid used in Madej et al. (2014), demonstrates the utility of reflection modeling to determine the emergent radius of multiple reflection features. It is unclear if the O and Fe line arising from a common emission radius within the accretion disk is unique to 4U 1543−624 or not, but through observing more UCXBs with NICER and NuSTAR, as well as with future X-ray missions like Athena (Nandra et al. 2013), HEX-P (Harrison et al. 2018), and STROBE-X (Ray et al. 2018), we can ascertain the accretion geometries of these systems.

Facilities: ADS, HEASARC, NICER, NuSTAR.

Software: HEAsoft (v6.27.2, HEASARC 2014), nustardas (v1.9.2), nicerdas (2020-04-23_V007a), xspec (v12.11.0, Arnaud 1996), Stingray (Huppenkothen et al. 2019).

ORCID iDs

R. M. Ludlam https://orcid.org/0000-0002-8961-939X
A. D. Jaodand https://orcid.org/0000-0002-3850-6651
J. A. García https://orcid.org/0000-0003-3828-2448
J. A. Tomsick https://orcid.org/0000-0001-5506-9855
E. M. Cackett https://orcid.org/0000-0002-8294-9281
A. C. Fabian https://orcid.org/0000-0002-9378-4072

References

Alabarta, K., Altamirano, D., Méndez, M., et al. 2020, MNRAS, 497, 3896
Arnaud, K. A. 1996, in ASP Conf. Ser. 101, Astronomical Data Analysis Software and Systems V, ed. G. H. Jacoby & J. Barnes (San Francisco, CA: ASP), 17
Bachetti, M., Harrison, F., Cook, R., et al. 2015, ApJ, 800, 109
Bailer-Jones, C. A. L., Rybizki, J., Fouesneau, M., et al. 2018, AJ, 156, 58
Ballantyne, D. R., Ross, R. R., & Fabian, A. C. 2002, MNRAS, 336, 867
Bogdanov, S., Guillot, S., Ray, P. S., et al. 2019, ApJL, 887, L25
Bult, P., Altamirano, D., Arzoumanian, Z., et al. 2018, ApJL, 860, L9
Cackett, E. M., Altamirano, D., Patruno, A., et al. 2009, ApJL, 694, L21
Cackett, E. M., Miller, J. M., Ballantyne, D. R., et al. 2010, ApJ, 720, 205
Cackett, E. M., Miller, J. M., Bhattacharyya, S., et al. 2008, ApJ, 674, 415
Choudhury, K., García, J. A., Steiner, J. F., & Bambi, C. 2017, ApJ, 851, 57
Dauser, T., Wilms, J., Reynolds, C. S., & Brenneman, L. W. 2010, MNRAS, 409, 1534
Degenaar, N., Altamirano, D., Parker, M., et al. 2016, MNRAS, 461, 4049
Degenaar, N., Pinto, C., Miller, J. M., et al. 2017, MNRAS, 464, 398
Di Salvo, T., D'Ai, A., Iaria, R., et al. 2009, MNRAS, 398, 2022
Di Salvo, T., Iaria, R., Matranga, M., et al. 2015, MNRAS, 449, 2794
Egron, E., Di Salvo, T., Motta, S., et al. 2013, A&A, 550, A5
Fabian, A. C., Iwasawa, K., Reynolds, C. S., & Young, A. J. 2000, PASP, 112, 1145
Fabian, A. C., Rees, M. J., Stella, L., & White, N. E. 1989, MNRAS, 238, 729
García, J., Dauser, T., Reynolds, C. S., et al. 2013, ApJ, 768, 146
Gendreau, K. C., Arzoumanian, Z., & Okajima, T. 2012, Proc. SPIE, 8443, 13
Harrison, F. A., Craig, W. W., Christensen, F. E., et al. 2013, ApJ, 770, 103
Harrison, F. A., Madsen, K. K., Grefenstette, B. W., et al. 2018, Proc. SPIE, 10699, 106992B
HEASARC, N. 2014, HEAsoft: Unified Release of FTOOLS and XANADU, v1.0, Astrophysics Source Code Library, ascl:1408.004
Hessels, J. W. T., Ransom, S. M., Stairs, I. H., et al. 2006, Sci, 311, 1901
Huppenkothen, D., Bachetti, M., Stevens, A. L., et al. 2019, ApJ, 881, 39
Juett, A. M., & Chakrabarty, D. 2003, ApJ, 599, 498
Koliopanos, F., Golfanov, M., & Bildsten, L. 2013, MNRAS, 432, 1264
Koliopanos, F., Peault, M., Vasilopoulos, G., & Webb, N. 2021a, MNRAS, 501, 548
Koliopanos, F., Vasilopoulos, G., Guillot, S., & Webb, N. 2021b, MNRAS, 500, 5603
Lin, D., Remillard, R. A., & Homan, J. 2007, ApJ, 667, 1073
Lodders, K. 2003, ApJ, 591, 1220
Ludlam, R. M., Cackett, E. M., García, J. A., et al. 2020, ApJ, 895, 45
Ludlam, R. M., Miller, J. M., Arzoumanian, Z., et al. 2018, ApJL, 858, L5
Ludlam, R. M., Miller, J. M., Bachetti, M., et al. 2017a, ApJ, 836, 140
Ludlam, R. M., Miller, J. M., Barret, D., et al. 2019a, ApJ, 873, 99
Ludlam, R. M., Miller, J. M., Cackett, E. M., et al. 2016, ApJ, 824, 37
Ludlam, R. M., Miller, J. M., Miller-Jones, J., & Reynolds, M. 2017b, ATel, 10690, 1
Ludlam, R. M., Shishkovsky, L., Bult, P. M., et al. 2019b, ApJ, 883, 39
Madej, O. K., García, J., Jonker, P. G., et al. 2014, MNRAS, 442, 1157
Madej, O. K., & Jonker, P. G. 2011, MNRAS, 412, L11
Miller, J. M. 2007, ARA&A, 45, 441
Miller, J. M., Parker, M. L., Fuerst, F., et al. 2013, ApJL, 779, L2
Mukherjee, D., Bult, P., van der Klis, M., & Bhattacharya, D. 2015, MNRAS, 452, 3994
Nandra, K., Barret, D., Barcons, X., et al. 2013, arXiv:1306.2307
Nelemans, G., & Jonker, P. G. 2010, NewAR, 54, 87
Nelemans, G., Jonker, P. G., Marsh, T. R., & van der Klis, M. 2003, MNRAS, 348, L7
Nelson, L. A., Rappaport, S. A., & Joss, P. C. 1986, ApJ, 304, 231
Papitto, A., Di Salvo, T., D'Aí, A., et al. 2009, A&A, 493, L39
Pinto, C., Kaastra, J. S., Costantini, E., & de Vries, C. 2013, A&A, 551, 25
Popham, R., & Sunyaev, R. 2001, ApJ, 547, 355
Ransom, S. M. 2001, PhD thesis, Harvard Univ.
Ransom, S. M., Eikenberry, S. S., & Middleditch, J. 2002, AJ, 124, 1788
Ray, P. S., Arzoumanian, Z., Brandt, S., et al. 2018, Proc. SPIE, 10699, 1069919
Sanna, A., Papitto, A., Burderi, L., et al. 2017, A&A, 598, A34
Savonije, G. J., de Kool, M., & van den Heuvel, E. P. J. 1986, A&A, 155, 51
Serino, M., Hiaka, K., Negoro, H., et al. 2018, ATel, 11302, 1
Shimura, T., & Takahara, R. 1995, ApJ, 445, 780
Strohmayer, T. E., Arzoumanian, Z., Bogdanov, S., et al. 2018, ApJL, 858, 13
Tetarenko, A. J., Bahramian, A., Wijnands, R., et al. 2018, ApJ, 854, 125
van den Eijnden, J., Degenaar, N., Pinto, C., et al. 2018, MNRAS, 475, 2027
Wang, J., Kara, E., Steiner, J. F., et al. 2020, ApJ, 899, 44
Wang, Z., & Chakrabarty, D. 2004, ApJL, 616, L139
Wang, Z., Tziamtzis, A., Kaplan, D. L., & Chakrabarty, D. 2015, PASA, 32, 35
Wilms, J., Allen, A., & McCray, R. 2000, ApJ, 542, 914